ACS APPLIED ENERGY MATERIALS

www.acsaem.org Article

Unusual Case of Higher Cyclic Stability at a Wider Voltage Window in Sodium Vanadium Phosphate

P. Laxman Mani Kanta, N. Lakshmi Priya, Prajeet Oza, M. Venkatesh, Satyesh Kumar Yadav, Bijoy Das,* G. Sundararajan, and R. Gopalan

Cite This: *ACS Appl. Energy Mater.* 2021, 4, 12581−12592 Read Online

ACCESS | Metrics & More | Article Recommendations | Supporting Information

ABSTRACT: NASICON-type $Na_3V_2(PO_4)_3$ is a promising cathode material for sodium-ion batteries (SIBs). However, large-scale synthesis of $Na_3V_2(PO_4)_3$ with a robust microstructure favoring enhanced sodium-ion storage, which is crucial for commercial usage as an electrode for SIBs, is still illusive. In this work, *in situ* carbon-coated $Na_3V_2(PO_4)_3$ (C-NVP) nanoparticles embedded in a three-dimensional mesoporous carbon matrix has been prepared by the scalable microwave-assisted sol−gel route. It delivers stable specific capacities of ∼112 and ∼102 mA h g^{-1} at 0.1 and 1 C-rates (1 C = 118 mA g^{-1}), respectively, in the potential window of 2.3−3.9 V *versus* Na/Na^+. In a wider potential window of 1.2−3.9 V, C-NVP shows reversible insertion/extraction of ∼2.4 moles of Na^+ ions corresponding to a specific capacity of ∼143 mA h g^{-1}, with 75% capacity retention after 500 cycles at 1.0 C-rate. We attribute such unusual stability at higher moles of Na^+-ion insertion to the ability of nanocrystallites to freely expand against mesoporous carbon as $Na_3V_2(PO_4)_3$ converts to $Na_4V_2(PO_4)_3$. Moreover, a symmetric full cell using C-NVP as both cathode and anode shows excellent cyclability and rate performance, with a high specific capacity of 50 mA h g^{-1} at 2 A g^{-1} stable for >10,000 cycles, corresponding to specific energy and power density of 88 W h kg^{-1} and 3504 W kg^{-1}, respectively. A proto-type pouch cell (symmetric full cell) delivers 7 mA h capacity at 0.1 A g^{-1}. The scalable microwave-assisted sol−gel route provides a robust solution for the large-scale synthesis of C-NVP with superior sodium-ion storage performance.

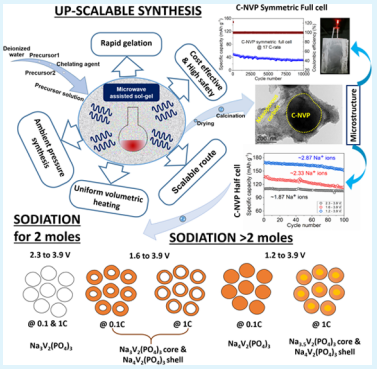

KEYWORDS: *microwave, sol−gel, $Na_3V_2(PO_4)_3$, mesoporous carbon, symmetric cell, sodium-ion battery*

1. INTRODUCTION

Sodium-ion batteries (SIBs) are getting great attention as promising secondary power sources for large-scale grid energy storage due to their low cost, abundance of sodium resources, and similar intercalation mechanism, resulting in on-par specific energy to lithium-ion batteries (LIBs).[1−4] In spite of various advantages, the lack of suitable cathode materials of a high specific energy and a long cycle life has delayed the commercialization of SIBs. In addition, the larger ionic radius of the Na^+ ion compared to the Li^+ ion brings down the sodium-ion transport kinetics, resulting in poor rate performance.[4,5] The materials having a large number of channels or interstitial space for sodium-ion transport can be employed as a suitable cathode for SIBs. Among different cathode materials, Na-super ionic conductor (NASICON)-type structures provide three-dimensional (3D) open frameworks with a large number of channels for faster sodium-ion transport.[6] In addition, they show better structural and thermal stability due to strong covalent bonding of the phosphate $(PO_4)^{3-}$ units.[1,2] NASICON-type $Na_3V_2(PO_4)_3$ (hereafter NVP) can be employed as a potential cathode owing to its high Na^+-ion intercalation potential (∼3.4 V *vs* Na^+/Na) with a theoretical specific capacity of 117.6 mA h g^{-1}.[6] The NVP framework consists of 3D $V_2(PO_4)_3$ units, in which VO_6 octahedra connect to the PO_4 tetrahedra through the corners, creating large interstitial sites for the Na^+ ions to diffuse.[7] However, NVP suffers from poor electronic conductivity, leading to inferior electrochemical performance, and hence is not suitable as a cathode for practical SIB applications.[8−10] Various synthesis routes have been adopted to prepare the NVP material with enhanced electronic conductivity through several conductive coating strategies.[7−18] Zhou *et al.* reported the synthesis of an irregular nanosheet-structured NVP material through a solid-state route using anthracite as carbon precursor, which showed 97.5 mA h g^{-1} at 5 C-rate.[11] A 3D interconnected carbon-coated NVP synthesized through hydrothermal route showed good performance due to enhanced sodium-ion transport kinetics.[12,13] The conventional sol−gel method has also been employed to synthesize the NVP−carbon composite, which showed a reversible capacity of 170 mA h g^{-1} between 0.01 and 3 V at 20 mA g^{-1}.[14] The

Received: August 6, 2021
Accepted: October 11, 2021
Published: October 25, 2021

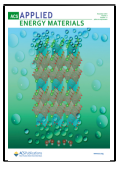

https://doi.org/10.1021/acsaem.1c02367
ACS Appl. Energy Mater. 2021, 4, 12581−12592

scalable aerosol spray process has been adopted to synthesize carbon-coated NVP porous hollow spheres, which showed 90% capacity retention at 20 mA g^{-1} after 300 cycles.[15] However, these synthesis routes involve various issues such as the formation of secondary phases (in the case of the solid-state route), low yield, being unsafe and expensive (in the case of hydrothermal or solvothermal), or inhomogeneous gelation due to a prolonged reaction time (conventional sol−gel).[16−18] Microwave radiation has been used extensively as a source of heat during material synthesis in either solid-state or solution-based routes.[19−21] The solution-based microwave synthesis yields nanomaterials at a shorter reaction time with improved functional properties (high purity) due to the lower activation energies and chemical homogeneity obtained from the localized super heating.[22−24] However, the issue of scalability arises for microwave-assisted hydrothermal or solvothermal synthesis, where pressure developed inside the reaction vessel leads to safety concerns. Moreover, microwaves have been used earlier for quicker drying of the gel formed by the conventional sol−gel method, which is not so beneficial.[25−28] The application of microwaves to the precursor solution in an open vessel can be an effective approach to synthesize the materials in a large scale through gelation within a very short time without any safety issues. However, there is no report on the microwave-assisted sol−gel synthesis of the C-NVP material to the best of our knowledge.

NVP has been mainly studied in the normal voltage window of 2−4 V *versus* Na/Na^+, which covers only the V^{3+}/V^{4+} redox couple, resulting in a low specific energy. However, reports on cycling in an extended voltage window of 1−4 V *versus* Na/Na^+ covering both V^{3+}/V^{4+} (∼3.4 V) and V^{3+}/V^{2+} (∼1.6 V) redox couples are limited. The two different voltage plateaus at ∼3.4 and ∼1.6 V correspond to the reversible insertion/extraction of >3 Na^+ ions, resulting in a specific capacity of >177 mA h g^{-1}.[29] Kang *et al.* have reported the cycling of polyol-assisted pyro-synthesized NVP in the extended potential window of 1.2−3.8 V *versus* Na^{+}/Na, where they have shown a specific capacity of 234 mA h g^{-1} for only 20 cycles.[30] Sequentially processed NVP, when cycled between 1 and 4 V at 0.5 C-rate showed dramatic fade in capacity after 20 cycles.[31] A similar cycling trend has been seen by Wei *et al.*, where they have reported capacity degradation from 200 to 10 mA h g^{-1} when cycled between 1 and 4 V.[29] Cycling in the full voltage window furnishes to utilize the reversible insertion/extraction of >3 Na^+ ions, which corresponds to a specific capacity of 177 mA h g^{-1}. Even though a very high specific capacity has been realized with cycling in an extended potential window, capacity degradation remains a big challenge, possibly due to structural disintegrity of the electrode material. The synthesis of nanostructured electrode materials with a robust microstructure can improve the cyclic stability by retaining the structural integrity.

Herein, we report the synthesis of *in situ* carbon-coated $Na_3V_2(PO_4)_3$ (hereafter C-NVP) embedded within the mesoporous carbon matrix through a scalable microwave assisted sol−gel route for Na^+-ion storage applications. A low-cost organic precursor (citric acid) was used as both chelating agent and source for carbon coating as well as for the 3D mesoporous carbon matrix. C-NVP shows excellent capacity retention of 92% after 500 cycles when cycled at 1.0 C-rate within 2.3−3.9 V *versus* Na^+/Na. Excellent electrochemical performance has also been noticed in an extended voltage window. At 1 C-rate, a high specific capacity of 143 mA h g^{-1} is seen with 75% of capacity retention after 500 cycles in the wide voltage window of 1.2−3.9 V. Higher cyclic stability with reversible insertion/extraction of ∼2.4 moles of Na^+ ions in the wide potential window of 1.2−3.9 V is attributed to the presence of a mesoporous carbon matrix which aids the NVP nanocrystallites to freely expand during the charge/discharge process. Lower capacity retention in the voltage window of 1.6−3.9 V has been understood in terms of poor kinetics of Na^+ ions in $Na_{1+x}V_2(PO_4)_3$ particles beyond 2 moles of Na^+-ion insertion. Excellent electrochemical performance of delivering a high specific energy of 88 W h kg^{-1} and power density of 3504 W kg^{-1} within 1.5 min have also been noticed when used as both a cathode and anode in a symmetric full cell with cyclic stability >10,000 cycles at 2.0 A g^{-1}.

2. EXPERIMENTAL SECTION

2.1. Material Synthesis. C-NVP was synthesized through a microwave-assisted sol−gel process. $NaH_2PO_4{\cdot}2H_2O$ (99%, Sigma-Aldrich), NH_4VO_3 (98%, Loba Chemie), and citric acid (99.5%, Sigma-Aldrich), with a molar ratio of 3:2:2, were used as the precursors during the synthesis. First, $NaH_2PO_4{\cdot}2H_2O$ was added to deionized water and ultrasonicated for 5 min until it was completely dissolved to form a clear solution. Further, NH_4VO_3 and citric acid were added to the solution sequentially under continuous stirring until a dark-reddish-colored transparent solution was obtained. The prepared solution was transferred to a microwave synthesizer (CEM Mars 6 Synthesis, USA), in which it was exposed to microwave radiation of maximum 400 W until 80 °C was reached. The gel was formed within 10 min of exposure to microwave radiation at 80 °C, followed by drying the gel at 120 °C in a hot air oven. The dried gel was ground and subjected to calcination by a series of heating at 400 °C for 4 h and 800 °C for 10 h in a tubular furnace under flowing argon gas to obtain a single-phase material. The experiment was carried out to prepare 30 g per batch and scaled up to 250−300 g per batch with consistent electrochemical performance using the existing facilities.

2.2. Structural Characterization. The structure of the as-synthesized C-NVP was characterized using a Rigaku Smart lab X-ray diffractometer with Cu Kα (1.5406 Å) radiation between 10 and 90° at a scan rate of 1° min^{-1}. The morphology and energy-dispersive spectroscopy (EDX) analyses were conducted by field emission scanning electron microscopy (FE-SEM) using a Carl Zeiss Merlin instrument at an accelerating voltage of 10 kV. Further, the morphology of the C-NVP composite was studied using a Technai G2 transmission electron microscope, having the LaB_6 filament with an electron beam of 200 kV. The lattice images were studied using an FEI TITAN D3300 high-resolution transmission electron microscope at an accelerating voltage of 300 kV. The infrared spectrum of the gel was recorded with attenuated total reflectance−Fourier transform infrared spectrometry (ATR−FTIR, Bruker VERTEX 70v) in the scan range of 50−4000 cm^{-1} under the transmission mode. Thermogravimetric analysis (TGA)/differential scanning calorimetry (DSC) was recorded on the synthesized gel using a Netzsch STA449 F1 Zupiter at a scan rate of 10 °C min^{-1} in an argon atmosphere. The carbon content in C-NVP has been estimated using a PerkinElmer 2400 CHNS−O analyzer. Confocal Raman images and spectra of C-NVP were recorded using an alpha 300 RAS WiTec spectrometer UHTS300 at a LASER excitation wavelength of 532 nm and 600 grooves mm^{-1} grating with a spectral center of 2100 rel cm^{-1}. The Brunauer−Emmet−Teller (BET) surface area of C-NVP was measured by nitrogen absorption−desorption technique using Micromeritics ASAP2020.

2.3. Computational Methods. Density functional theory (DFT) calculations were performed using the Vienna ab initio simulation package (VASP) with projector-augmented wave (PAW) pseudopotentials. The calculations employed the Perdew, Burke, and Ernzerhof (PBE) generalized gradient approximation (GGA) exchange correlation functional with Hubbard U-corrections and rotationally

https://doi.org/10.1021/acsaem.1c02367
ACS Appl. Energy Mater. 2021, 4, 12581−12592

Scheme 1. Schematic Diagram of Microwave-Assisted Sol−Gel Synthesis, Followed by Calcination to Prepare the Mesoporous Carbon-Encapsulated $Na_3V_2(PO_4)_3$ Nanocomposite

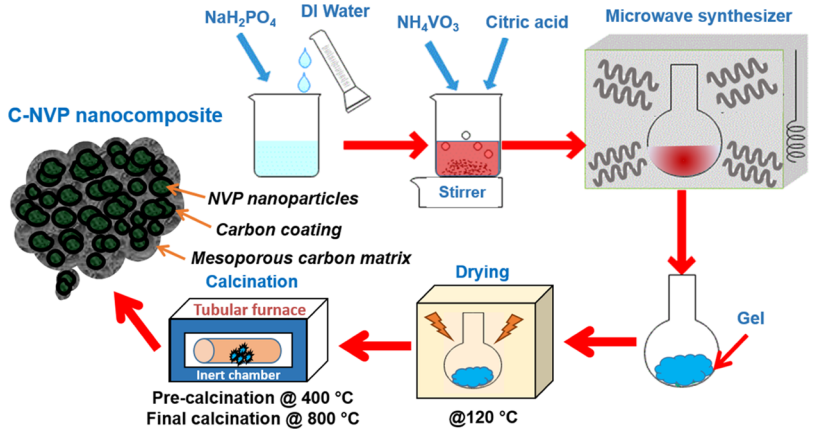

invariant approach. The value of 4.2 eV as U_{eff} was used for the vanadium ion as suggested by Lim *et al.*[32] All the calculations employed a plane wave basis with an energy cutoff of 520 eV and 4 × 4 × 2 Monkhorst−Pack mesh for *k*-point sampling for all converged results. Hereafter, the different stoichiometries of $Na_xV_2(PO_4)_3$ are represented as Na*x*VP (x = 0 to 4), where Na ions sit in two crystallographic sites, namely, the 6b site and 18e site, commonly referred to as Na(1) and Na(2), respectively. For Na1VP, all 6b sites were filled. To create structures with more Na atoms, filling of Na(2) sites was carried in a way so that there is minimum electrostatic repulsion between Na ions. To do so, one of the Na(2) sites is chosen as the starting point. The next site chosen was farthest from the first site. Similarly, the average distance between next sites from the previously chosen site was the largest. Also, this process continues until all the sites are filled. Occupancies of Na(1) and Na(2) sites for various stoichiometric structures are provided in Supporting Information, Table S1.

To understand relative stability of various stoichiometries, we calculate the formation energy of Na*x*VP with Na0VP and Na4VP as references

$$\Delta E_f(\mathrm{Na}x\mathrm{VP}) = E(\mathrm{Na}x\mathrm{VP}) - \frac{(4-x)}{4}E(\mathrm{Na0VP}) - \frac{x}{4}E(\mathrm{Na4VP}) \quad (1)$$

where E(Na*x*VP), E(Na0VP), and E(Na4VP) are the DFT energies of $Na_xV_2(PO_4)_3$, $V_2(PO_4)_3$, and $Na_4V_2(PO_4)_3$, respectively. The Hull plot is constructed by drawing formation energy *versus* composition, which conceptualizes the formation of mixed stoichiometry based on the two stable stoichiometries that are taken as references. The mixed stoichiometry is represented as a convex combination of the reference ones. The stable stoichiometry falls on the Hull plot, while the unstable stoichiometry falls above the Hull plot.

2.4. Electrochemical Characterization. For electrode preparation, a homogeneous slurry was made by thorough mixing of as-prepared C-NVP, carbon black, and the polyvinylidene fluoride (PVDF) binder in a weight ratio of 80:13:7. *N*-Methyl-2-pyrrolidone (NMP) was used as a solvent for the PVDF binder. The slurry was coated onto an aluminum current collector (AA1060, Gelon, 25 μm thick) using a doctor blade. The coated electrode was further dried at 80 °C for 24 h in a vacuum oven (Binder GmbH), followed by calendaring at a pressure of 3000 psi. 2032-type coin cells were fabricated using the C-NVP electrode as a cathode against sodium metal as the reference/counter electrode using in-house prepared 1 M $NaClO_4$ in EC/PC (1:1 by vol %) as the electrolyte and glass microfiber filters (Whatmann GF/D) as a separator. The as-prepared electrolyte has an ionic conductivity of 7.54 mS cm^{-1} at 27 °C measured using a Metrohm 914 pH/Conductometer. In addition, the symmetric cell consisting of C-NVP as both cathode and anode was fabricated for its performance evaluation. The symmetric pouch cell was fabricated using electrodes of dimensions of 73 × 43 mm (length × width) with a loading weight of 3.8 mg cm^{-2} using polypropylene as a separator and a polymer-laminated aluminum sheet as a pouch material. The electrode preparation and cell fabrication were carried out inside an argon-filled glovebox, where H_2O and O_2 were maintained at <0.1 ppm. Electrochemical characterization of the C-NVP electrode in the half- and full-cell modes was conducted by cyclic voltammetry (CV) and galvanostatic cycling with potential limitation (GCPL) techniques using biologic (BCS-810) and Arbin (BT2000) battery testers under different testing conditions, respectively. Electrochemical impedance spectroscopy (EIS) was conducted on C-NVP using an AMETEK PARSTAT MC electrochemical work station at an applied AC voltage amplitude of 10 mV between 10^6 and 10^{-1} Hz.

3. RESULTS AND DISCUSSION

Scheme 1 shows the schematic diagram of the detailed synthesis procedure for gel formation with the exposure of microwave radiation, followed by calcination to achieve *in situ* carbon-coated $Na_3V_2(PO_4)_3$. Here, an open vessel-based microwave-assisted sol−gel synthesis has been employed, where sodium dihydrogen phosphate ($NaH_2PO_4{\cdot}2H_2O$) was dissolved initially in deionized water, which dissociated into Na^+ and $H_2PO_4^-$ ions, resulting in a transparent colorless solution. With the addition of ammonium metavanadate (NH_4VO_3), the solution changed to transparent yellow containing dissociated NH_4^+ and VO_3^- ions where vanadium is in the +5 oxidation state. Finally, addition of citric acid ($C_6H_8O_7$), the chelating agent, results in a dark-red-colored transparent solution where the pH was around 4.5. The highly oxidizing nature of VO_3^- in the acidic medium (pH < 7) has oxidized some part of $C_6H_8O_7$ to $C_5H_6O_5$.[12] With exposure to microwave radiation maintained at 80 °C, the rapid hydrolysis of Na^+, $H_2PO_4^-$, NH_4^+, and VO_3^- occurred in the presence of a chelating/reducing agent to form NaOH, H_3PO_4, NH_4OH, and $VO(OH)_2$, where vanadium has been reduced to the +4 oxidation state.

The detailed chemical reactions have been discussed in Supporting Information (Equations S1−S9). The polycondensation occurred with the aid of carbonyl groups of both $C_5H_6O_5$ and $C_6H_8O_7$ chelators at the expense of rapid evaporation of the solvent at 80 °C. An ultrafast gelation (≤10 min) resulted in a blue-colored gel representing the oxidation state of vanadium as +4. The gel formed after the chelation process by the interaction of VO^{2+} with the chelators having

https://doi.org/10.1021/acsaem.1c02367
ACS Appl. Energy Mater. 2021, 4, 12581−12592

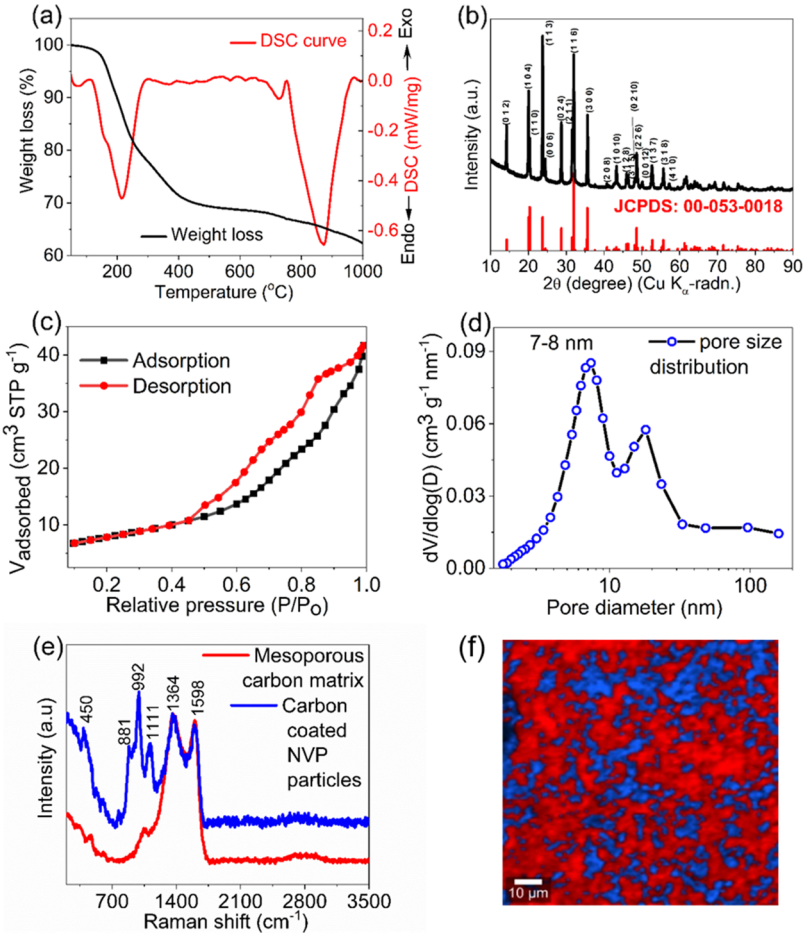

Figure 1. (a) TGA and DSC plots of NVP gel in an argon atmosphere. (b) X-ray diffraction pattern of the C-NVP material. (c) BET surface area plot. (d) BJH pore size distribution. Confocal Raman spectroscopy of (e) C-NVP particles embedded in the mesoporous carbon matrix; and (f) combined distribution showing C-NVP particles (blue) in the mesoporous carbon matrix (red).

carboxyl bonds (C═O) has been evidenced from the ATR−FTIR spectrum as given in Supporting Information (Figure S1). The calcination temperatures are determined from the TGA data of the gel where major weight losses are seen. The TGA plot depicts major weight losses in the temperature range of 140 to 400 °C, followed by minor weight losses until 1000 °C (Figure 1a). Based on the TGA data, the first-step calcination has been carried out at 400 °C to remove all the volatile compounds and to ensure the decomposition of citric acid to form amorphous carbon. Further calcination at 800 °C was performed to reduce V^{4+} to V^{3+} through *in situ* carbothermal reduction and crystallization of $Na_3V_2(PO_4)_3$. Part of the carbon formed during initial calcination acts as a reducing agent. Such reduction of V^{4+} to V^{3+} at 800 °C is supported by the weight loss and endothermic peak in the temperature range of 700 to 900 °C (Figure 1a).

Figure 1b depicts the powder XRD pattern of the synthesized C-NVP material. All the observed peaks due to NVP are well indexed to the NASICON-type rhombohedral crystal structure with the $R\bar{3}c$ space group (JCPDS Card no. 00-053-0018).[13,33,34] No peaks due to the secondary phase are observed. The ascertained peaks are slightly broadened in spite of the high synthesis temperature, indicating nanocrystalline nature of the synthesized NVP particles with a crystallite size of 55 ± 2 nm as calculated from the Scherrer equation.[35] The amount of carbon present in the material is found to be 5.83% from CHNS−O analysis. The optimum percentage of carbon present in this nanocomposite is lesser than most of the earlier reports, and a comparison table is given in Supporting Information (Table S2). A lower carbon content is preferred in order to increase the specific energy with respect to the total weight as carbon is electrochemical-inactive in the cycling range of a cathode. Figure 1c shows the Brunauer−Emmett−Teller (BET) isotherms of C-NVP, indicating a type IV adsorption mechanism of N_2 gas.[36] The BET surface area is found out to be 27.7 $m^2\ g^{-1}$ with the pore size distribution in the range of 7−8 nm, conveying the mesoporous nature of the carbon present in the C-NVP material (Figure 1c,d). Figure 1e shows the Raman spectrum of C-NVP powder, where various bands at 450, 881, 992, and 1111 cm^{-1} due to NVP are seen along with the bands of mesoporous carbon at 1364 cm^{-1} (D-band) due to sp^3 hybridization and 1598 cm^{-1} (G-band) due to sp^2 hybridization. Raman bands between 150 and 1200 cm^{-1} represent the vibrational or bending modes of VO_4 or PO_4 polyhedra of NVP. The intense energy bands observed at 1111 and 992 cm^{-1} represent the asymmetric and symmetric stretching modes of PO_4^{3-}, respectively. The energy band due to V−O vibration in VO_4^{3-} is observed at 881 cm^{-1}. The weak energy band due to the P−O bending mode in PO_4^{3-} is noticed at 450 cm^{-1}.[12] The I_D/I_G ratio obtained from the Raman spectrum of carbon (Figure 1e) was found to be 1.103, indicating the disordered nature of carbon obtained from the decomposition of citric acid.[37] The combined distribution of confocal Raman imaging taken on the C-NVP pellet has shown

https://doi.org/10.1021/acsaem.1c02367
ACS Appl. Energy Mater. 2021, 4, 12581−12592

a clear distribution of C-NVP particles within the mesoporous carbon matrix, where the blue and red zones represent C-NVP particles and the mesoporous carbon matrix, respectively (Figure 1f). The mesoporous carbon encapsulation on NVP particles greatly improves the electronic conductivity of the composite material, leading to enhanced electrochemical performance.

Figure 2a,b shows FE-SEM images of as-prepared C-NVP powder at different magnifications. FE-SEM image at a lower magnification (Figure 2a) depicts the NVP nanoparticles with an irregular shape and size ranging from 300 to 500 nm. At a higher magnification, it is noticed that the NVP nanoparticles with a particle size of 100−150 nm agglomerated to form the particles of a sub-micron size (Figure 2b). EDX analysis showed a uniform distribution of Na, V, P, and O with elemental mapping (Supporting Information, Figure S2). Further, TEM analysis depicts the distribution of NVP nanoparticles within the mesoporous carbon matrix (Figure 2c,d), supporting the confocal Raman imaging (Figure 1e,f). The pores present in the gel not only acted as nucleating sites for NVP nanoparticles but also restrained their growth in order to achieve a controlled particle size, which is confirmed from the TEM images (Figure 2c,d). Such a microstructure of embedded NVP nanoparticles within the mesoporous carbon matrix provided continuous transport paths for sodium ions to diffuse three-dimensionally. The coral-like mesoporous carbon network also aids in easy percolation of the electrolyte during electrochemical cycling, which enhances the accessibility of the active material. The high-resolution transmission electron microscopy (HR-TEM) image depicts clear lattice fringes of different inter-planar distances, indicating different orientation of NVP crystallites. The inter-planar distances of 0.37 and 0.44 (±0.02) nm between two fringes represent (113) and (104) planes, respectively, as shown in Figure 2e,f. A uniform carbon coating of a thickness <10 nm, which is obtained due to the decomposition of citric acid, is depicted from the HR-TEM images, as shown in Figure 2f.

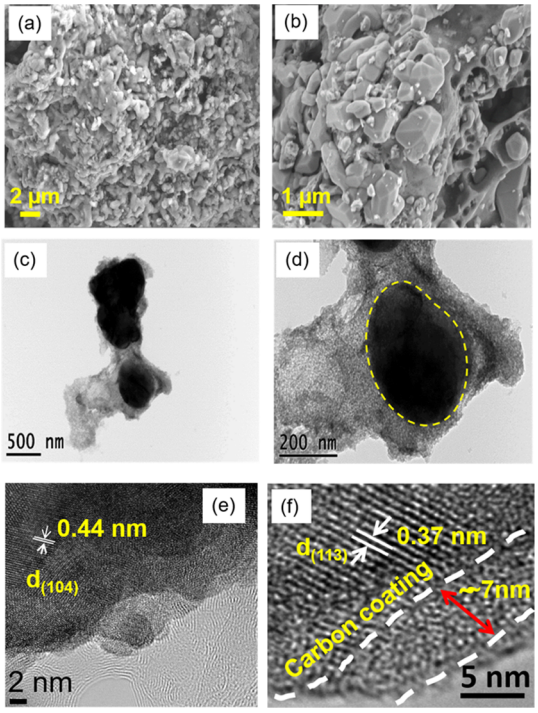

Figure 2. (a,b) FE-SEM images of C-NVP nanoparticles at different magnifications. (c,d) TEM images showing C-NVP nanoparticles embedded within the mesoporous carbon matrix. (e,f) HRTEM lattice images of C-NVP nanoparticles showing carbon coating.

Cyclic voltammetry (CV) was performed on the C-NVP cathode against Na-metal as the reference electrode to determine the electrochemical-active redox couples. Figure 3a shows the CV plots of the first cycle to the fifth cycle swept between 2.3 and 3.9 V at a scan rate of 100 μV s^{-1}. During the charge process, a sharp and well-defined peak is noticed at ~3.45 V, which represents the Na^+-ion extraction from the $Na_3V_2(PO_4)_3$ structure, leading to the oxidation of V^{3+} to V^{4+}. Unlike the charge process, two distinct peaks are noticed at ~3.34 and ~3.25 V during discharge, which are due to the reduction of V^{4+} to V^{3+}. The splitting of the peak is due to the local arrangement of sodium ions in the structure, possibly the migration from Na(1) to the Na(2) site. Such phenomena are commonly observed in NASICON-type structures.[6,38−41] At a higher cycle number (fifth cycle), the peak intensity at ~3.25 V remained almost same, indicating the reversibility of Na^+-ion migration from Na(1) to the Na(2) site, which contributes to the total discharge capacity. The CV profile of C-NVP in a wide range of the potential window of 1.0−3.9 V depicts an additional reversible redox couple at ~1.67 V (due to V^{3+}/V^{2+}) and at ~1.7 V (due to V^{2+}/V^{3+}) during the discharge and charge processes, respectively (Figure S4).

The first-cycle galvanostatic charge/discharge plots of C-NVP in different voltage windows at a 0.1 C-rate are shown in Figure 3b. The charge profile of C-NVP, when cycled between 2.3 and 3.9 V, shows a flat voltage plateau at ~3.4 V due to V^{3+}/V^{4+}, similar to that of CV (Figure 3a). The specific capacity of 112 mA h g^{-1} is observed at the end of charge (3.9 V), which corresponds to the extraction of ~1.9 moles of Na^+ ions from the NVP structure (eq 2). The following discharge curve also exhibits a flat voltage plateau at ~3.3 V with a voltage hysteresis of ~0.1 V, which is lower compared to that of other cathode materials.[8,10,37] At the end of the first discharge, a high specific capacity of ~110 mA h g^{-1} is observed with 98% of coulombic efficiency. With lowering of the cutoff voltage to 1.6 and 1.2 V, further insertion of Na^+ is observed into the NVP structure, thereby increasing the specific capacity. When cycled down to 1.6 and 1.2 V, C-NVP has shown higher discharge specific capacities of 137 and 169 mA h g^{-1} at a 0.1 C-rate (Figure 3b) with first-cycle coulombic efficiencies of 96 and 97%, respectively. The observed specific capacities correspond to insertion of ~2.33 and ~2.87 moles of Na^+ ions into the NVP structure, respectively (eqs 4, 5). The reduction of V^{3+} to V^{2+} at ~1.67 V facilitates reversible insertion of nearly one more Na^+ ion into the $Na_3V_2(PO_4)_3$ structure to form $Na_4V_2(PO_4)_3$. The overall electrochemical reactions have been proposed based on the observed reversible specific capacities at various lower cutoff voltages as follows:

During the first charge:

$$Na_3V_2(PO_4)_3 \xleftrightarrow{\text{charge}} Na_{1.1}V_{1.9}^{4+}V_{0.1}^{3+}(PO_4)_3 + 1.9Na^+ + 1.9e^- \quad (2.3 - 3.9\ \text{V}) \tag{2}$$

During the first discharge:

https://doi.org/10.1021/acsaem.1c02367
ACS Appl. Energy Mater. 2021, 4, 12581−12592

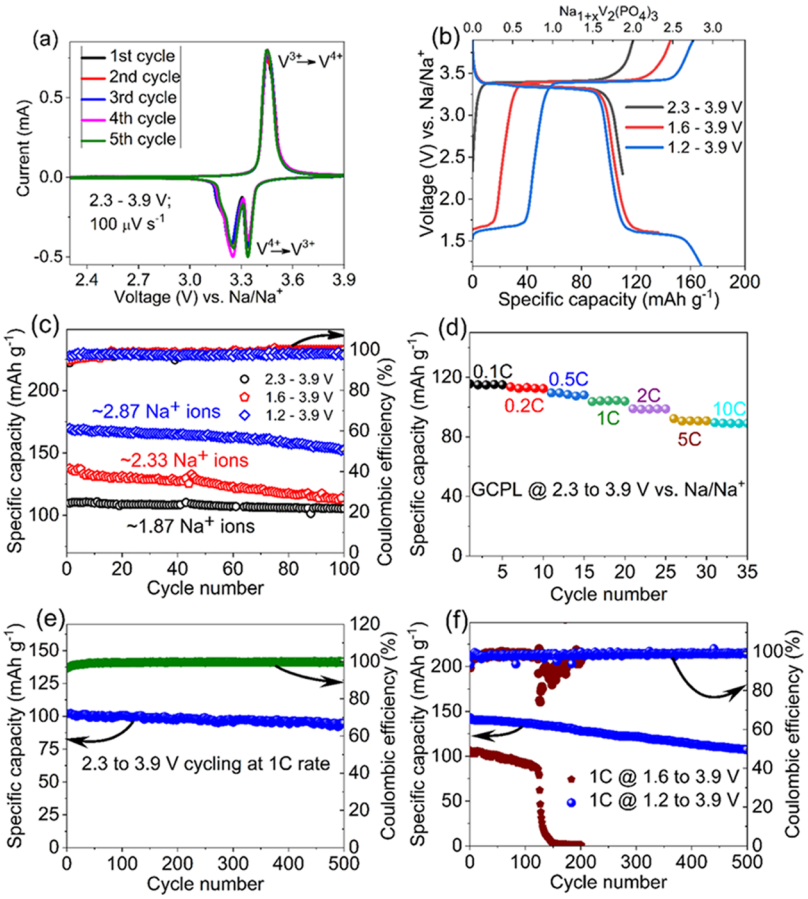

Figure 3. (a) Cyclic voltammograms of C-NVP at 100 μV s^{-1} scan rate; (b) galvanostatic charge/discharge plots of C-NVP at 0.1 C-rate (1 C = 118 mA g^{-1}) in different voltage windows. Specific capacity *vs* cycle number plots of C-NVP (c) at 0.1 C-rate and (d) at different C-rates. Specific capacity *vs* cycle number plots at 1.0 C-rate, (e) 2.3−3.9 V *vs* Na^+/Na and (f) 1.6−3.9 V and 1.2−3.9 V *vs* Na^+/Na.

$$Na_{1.1}V_{1.9}^{4+}V_{0.1}^{3+}(PO_4)_3 + 1.87Na^+ + 1.87e^- \xrightleftharpoons{\text{discharge}} Na_{2.97}V_{0.03}^{4+}V_{1.97}^{3+}(PO_4)_3 \quad (2.3 - 3.9\ V) \tag{3}$$

$$Na_{1.1}V_{1.9}^{4+}V_{0.1}^{3+}(PO_4)_3 + 2.33Na^+ + 2.33e^- \xrightleftharpoons{\text{discharge}} Na_{3.43}V_{0.43}^{2+}V_{1.57}^{3+}(PO_4)_3 \quad (1.6 - 3.9\ V) \tag{4}$$

$$Na_{1.1}V_{1.9}^{4+}V_{0.1}^{3+}(PO_4)_3 + 2.87Na^+ + 2.87e^- \xrightleftharpoons{\text{discharge}} Na_{3.97}V_{0.97}^{2+}V_{1.03}^{3+}(PO_4)_3 (1.2 - 3.9\ V) \tag{5}$$

Figure 3c depicts the capacity *versus* cycle number plot for C-NVP cycled within different voltage windows at 0.1 C-rate. When cycled within 2.3−3.9 V, it exhibits a high reversible specific capacity of ∼112 mA h g^{-1} without any noticeable capacity degradation up to 100 cycles with 99% retention. Excellent rate performance is also seen when cycled at various current rates (Figure 3d), with high specific capacities of 112, 110, 109, 102, 99, 90, and 89 mA h g^{-1} at 0.1, 0.2, 0.5, 1.0, 2.0, 5.0, and 10 C-rates, respectively, in the voltage window of 2.3−3.9 V *versus* Na^+/Na. At 1.0 C-rate, it still exhibits ∼102 mA h g^{-1} with 92% of capacity retention after 500 cycles (Figure 3e). In extended voltage windows of 1.2−3.9 and 1.6−3.9 V, when cycled at 0.1 C-rate, it delivers high reversible capacities of 169 and 137 mA h g^{-1} with 90 and 82% capacity retention after 100 cycles, respectively (Figure 3c). Cycling at 1 C-rate in the extended voltage window of 1.2−3.9 V shows a high specific capacity of 143 mA h g^{-1} with capacity retention of 75% after 500 cycles (Figure 3f). In the case of 1.6−3.9 V, only 107 mA h g^{-1} specific capacity is noticed, which drastically fades after 100 cycles (Figure 3f). In this study, an unusual cyclic stability has been noticed when deeply cycled between 1.2 and 3.9 V rather than 1.6−3.9 V. Although there are reports on a high specific capacity of >150 mA h g^{-1} in the wide voltage window, the gradual fade in capacity has been noticed with <10% capacity retention after a certain number of cycles. The reason for such capacity degradation has been explained in terms of huge volume expansions or biphasic phase transformations.[29,31] To the best of our knowledge, there is only one report on dual nitrogen-doped carbon-decorated NVP embedded in the expanded rGO (NVP@C/rGO-U) composite, exhibiting 89% capacity retention after 100 cycles at 1 C-rate.[42] In our work, a simple mesoporous carbon-encapsulated NVP (C-NVP) nanocomposite even showed better capacity retention of 93% after 100 cycles at 1 C-rate (Figure 3f). The presence of mesoporous carbon provides additional electronic conductivity, whereas the pores allow the easy percolation of the electrolyte, promoting faster Na^+-ion transport.[41,43] Such a microstructure is beneficial, which helps to prevent any structural changes and electrode degradation while minimizing the physical contact with the electrolyte through carbon coating. The electrochemical impedance spectroscopy (EIS) measurements on fresh and cycled C-NVP (after 200 cycles at

https://doi.org/10.1021/acsaem.1c02367
ACS Appl. Energy Mater. 2021, 4, 12581−12592

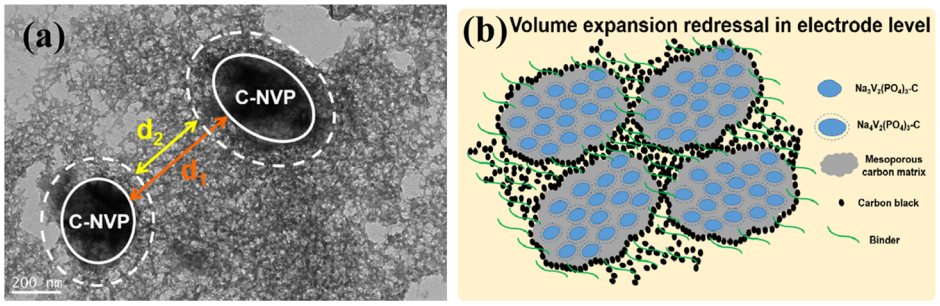

Figure 4. (a) TEM image showing the typical inter-particle distance (d_1 is 489 nm) in as-prepared Na3VP. Also shown is the typical separation when particles expand when Na4VP forms represented by a broken line (d_2 is 465 nm based on assumption that particles are spherical). (b) Representation of Na3VP particles embedded in the mesoporous carbon matrix dispersed in carbon black and the binder in the electrode level.

1.0 C) further support such explanation. The Nyquist plots of C-NVP before and after cycling shown in Figure 6d depict minor change in charge-transfer resistance, and it remained almost the same even after 200 charge/discharge cycles.

The unusual cycling behavior of C-NVP with higher capacity retention when cycled between 1.2 and 3.9 V compared to that of 1.6−3.9 V has been explained with the help of both experimental and theoretical (DFT) data. Figure 4a depicts the TEM image indicating the typical inter-particle distance of as-prepared Na3VP along with the distances when particles have changed to Na4VP. The change in distance when Na3VP converts to Na4VP was estimated by assuming particles to be spherical. Twice the change in radius of the particle is taken as the change in distance on conversion. Volumes per formula unit as calculated from DFT are listed in Table 1, which are used to estimate the volume change of particles. It confirms that particles can freely expand in the amorphous carbon matrix without exerting stress on each other, hence achieving high-capacity retention. Figure 4b shows the schematic representation of Na3VP particles embedded in the mesoporous carbon matrix (secondary particles) dispersed in carbon black and the binder in the electrode level, confirming how particle expansion takes place without the straining binder, which has been suggested as a reason of failure in previous studies.[31]

Table 1. Calculated Volume Change at Different Sodiation Levels

composition	volume of the unit cell (Å^3)	change in volume w.r.t Na1VP (%)
Na1VP	1390.26	0
Na3VP	1487.58	6.5
Na3.5VP	1513.04	8.1
Na4VP	1532.87	9.3

At 0.1 C-rate, after 100 cycles, we find capacity retention of 90% when cycled between 1.2 and 3.9 V, with an initial specific capacity of ∼169 mA h g^{-1}, compared to 82% capacity retention when cycled between 1.6 and 3.9 V, with an initial specific capacity of ∼137 mA h g^{-1}. This behavior is counterintuitive to the well-established notion that a larger amount of ion cycling results in poor cyclic stability. A similar discrepancy was observed by Ceder *et al.*, where they observe poor cyclic stability in the voltage window of 1.5−4.5 V compared to 1.0−4.5 V in $NaMnCr(PO_4)_3$, but no explanation was provided.[44] We explain the origin of higher stability at a wider cyclic window in terms of the barrier associated with bulk diffusion of Na$^+$ ions in particles and the driving force for intercalation of Na$^+$ into the particle. The driving force for intercalation is dictated by the voltage; lower the voltage, higher the driving force. The barrier to diffusion may change as the concentration of Na$^+$ present in the particle changes. Figure 3c lists capacity retentions in various voltage windows at 0.1 C-rate. When cycled between 2.3 and 3.9 V, cyclic stability is very high compared to cycling at a wider voltage window at both 0.1 and 1 C-rates. This is due to the low barrier to diffusion of Na$^+$ ions as the concentration of Na ions is low, which in turn results in uniform distribution of Na ions throughout the particles (Figure 5a). However at a lower voltage, the stoichiometry of particles has to reach $Na_{3+x}V_2(PO_4)_3$. Insertion of more than 2 Na$^+$ in Na1VP results in a larger barrier to diffusion. Also, their thermodynamic stability decreases compared to that of Na3VP, which is the most stable stoichiometry as shown in Figure S5. Through CV, we established that under very slow charging, Na4VP formation can be achieved at 1.67 V in the half cell (Figure S4). As the cell is cycled between 1.6 and 3.9 V, although the voltage is low enough to form Na4VP; however it is not sufficient enough to diffuse Na$^+$ fast to form Na4VP throughout the particle. This results in the formation of the

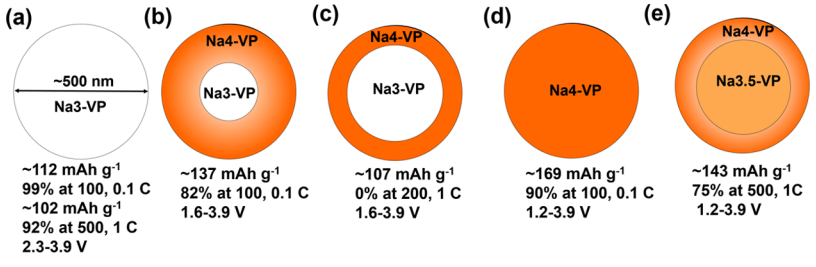

Figure 5. Representation of concentration of Na ions in discharged particles at various cycling windows and capacity retention at the number of cycles.

https://doi.org/10.1021/acsaem.1c02367
ACS Appl. Energy Mater. 2021, 4, 12581−12592

Na4VP shell and Na3VP core leading to the lattice mismatch between the core and shell, and hence the particle loses stability (Figure 5b). An even sharp separation between the Na4VP shell and Na3VP core emerges when cycled at 1 C, as shown in Figure 5c, resulting in total deterioration of the particle after 200 cycles (Figure 3f). On the other hand, in the 1.2−3.9 V cycling window, as the driving force for diffusion of Na^+ ions is higher at a slower rate of 0.1 C, a uniform distribution of Na^+ ions occurs, resulting in better stability (Figure 5d). At a higher charging rate of 1 C, the core−shell-type structure forms, resulting in poor stability, but as the lattice mismatch between the core and shell is less due to the formation of Na3.5VP in the core region, it results in better stability (Figure 5e).

The CV measurements at different scan rates were performed on C-NVP *versus* the Na/Na^+ system to understand the Na^+-ion transport mechanism, and the profiles at various scan rates (0.1−2.0 mV s^{-1}) are shown in Figure 6a. It is

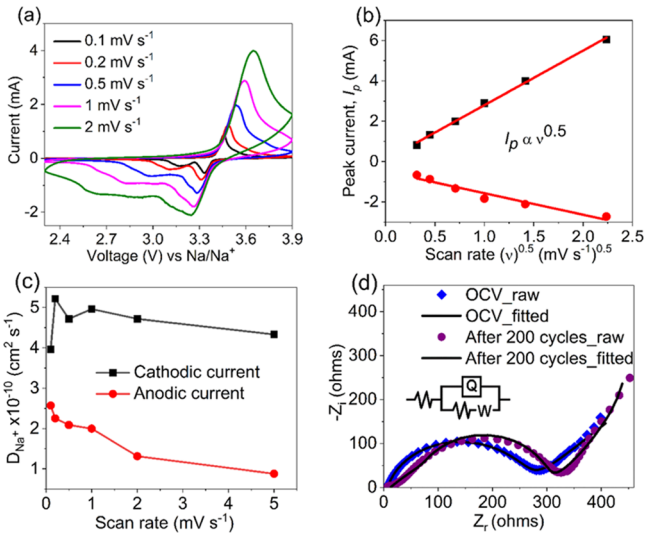

Figure 6. (a) Cyclic voltammograms of C-NVP at different scan rates in the voltage window of 2.3−3.9 V *vs* Na/Na^+. (b) Peak current *vs* square root of scan rate plots of C-NVP. (c) Diffusion coefficient *vs* scan rate plot of C-NVP. (d) Nyquist plots of C-NVP in a half cell before and after cycling at 1.0 C-rate.

noticed that peaks due to the reduction (cathodic) and oxidation (anodic) processes are shifted. With the increase in scan rates, the peak current (I_p) has been increased during both the processes. It was found that the current measured during the oxidation process is higher than that of the current measured during reduction, indicating little difference in the kinetics of Na^+-ion insertion and the extraction process. Figure 6b shows the plots of peak current (I_p) *versus* square root of scan rates during the redox process. The peak current in both the processes followed a linear relationship to the square root of the scan rate ($\nu^{0.5}$), implying the transportation of Na^+ ions *via* solid-state diffusion. A similar Na^+-ion storage mechanism has also been reported for other electrode materials, when cycled against Na metal.[37−39]

The chemical diffusion coefficient of the Na^+ ion (D_{Na^+}) was determined from the CV plots (Figure 6a) recorded at different scan rates, and the data are shown in Figure 6c. The D_{Na^+} values were calculated by measuring the peak current along with other parameters using the Randles−Sevcik's equation[45,46]

$$i_p = 2.69 \times 10^5 \sqrt[3]{n} AC \sqrt{D_{Na^+} \nu} \quad (6)$$

where i_p is the peak current (A), n is the number of electrons transferred during reaction, F is the Faraday constant (96486 C mol^{-1}), C is the concentration of Na^+ ions (mol cm^{-3}), A is the surface area of the electrode (cm^2), D_{Na^+} is the chemical diffusion coefficient (cm^2 s^{-1}) of the Na^+ ion, and ν is the scan rate (V s^{-1}). The calculated D_{Na^+} values are in the range of $3.97-5.22 \times 10^{-10}$ cm^2 s^{-1}. Such a high diffusion coefficient is possibly due to the synergetic effect of the mesoporous carbon microstructure and nanoscale nature of the NVP material.

The electrochemical performance of as-prepared C-NVP was further investigated in the symmetric full cell owing to the two different redox couples of vanadium, where C-NVP was used as both cathode and anode. In the symmetric full cell, based on the vanadium redox couple (V^{3+}/V^{2+}), the following reactions are possible:

At the cathode,

$$Na_3V_2(PO_4)_3 \xleftrightarrow{\text{charge}} NaV_2(PO_4)_3 + 2Na^+ + 2e^- \quad (7)$$

At the anode,

$$Na_3V_2(PO_4)_3 + 2Na^+ + 2e^- \xleftrightarrow{\text{charge}} Na_5V_2(PO_4)_3 \quad (8)$$

The cyclic voltammogram of C-NVP *versus* Na/Na^+ at lower voltages showed a redox peak at 0.4 V, confirming the further sodiation up to 5 Na^+ ions (Figure S6). After complete occupation of 6b (Na1) and 18e (Na2) crystallographic sites, Na^+ ions occupy 6a sites of the unit cell when the fifth sodium is inserted. Jian *et al.* have reported that the occupation of 6a sites at lower voltages was due to huge coulombic repulsions experienced by the Na^+ ions which demand more energy to overcome the barrier.[47] Based on this reversible shuttling of 2 Na^+ ions in the symmetric full cell, the cathode to anode weight ratio is maintained as 1, whereas the loading of both the electrodes are taken as 1.5 mg cm^{-2}each. Figure 7a depicts the CV profile for C-NVP symmetric cell cycled at 100 μV s^{-1}, whereas intense oxidation and reduction peaks centred at ~1.67 and ~1.85 V are noticed, with an average voltage of 1.76 V, which is almost same as the expected value on the basis of the voltage difference between the V^{3+}/V^{4+} (~3.4 V) and V^{3+}/V^{2+} (~1.67 V) in $Na_3V_2(PO_4)_3$ (Figure S4). The C-NVP symmetric full cell exhibited an output voltage of ~1.8 V. The galvanostatic charge/discharge profiles of the C-NVP symmetric full cell at 0.1, 1, and 2 A g^{-1} (equivalent to 0.85, 8.5, and 17 C-rates based on the capacity calculation of 1 C = 118 mA h g^{-1}) are shown in Figure 7b,c. The time taken for completing a full cycle at 1, 2, and 5 A g^{-1} is 6.6, 3, and 1.2 min, respectively (Figure 7b). At the end of the first discharge, ~90 mA h g^{-1} is noticed at 0.85 C (Figure 7d), corresponding to the high specific energy of ~157 W h kg^{-1}, which is higher than that reported in the literature on symmetric SIBs to the best of our knowledge.[48−56] The performance of the C-NVP symmetric full cell at 1 and 2 A g^{-1} (8.5 and 17 C) shows a similar voltage plateau with a slight increase in voltage polarization (ΔV = 0.12 and 0.42 V). The reversible specific capacity of ~60 and ~50 mA h g^{-1} with an excellent cyclic stability is noticed with capacity retention of 88.4 and 65% after 1400 and 10,000 cycles, respectively (Figure 7d,e). The relatively high specific energy of 106 W h kg^{-1} has been

https://doi.org/10.1021/acsaem.1c02367
ACS Appl. Energy Mater. 2021, 4, 12581−12592

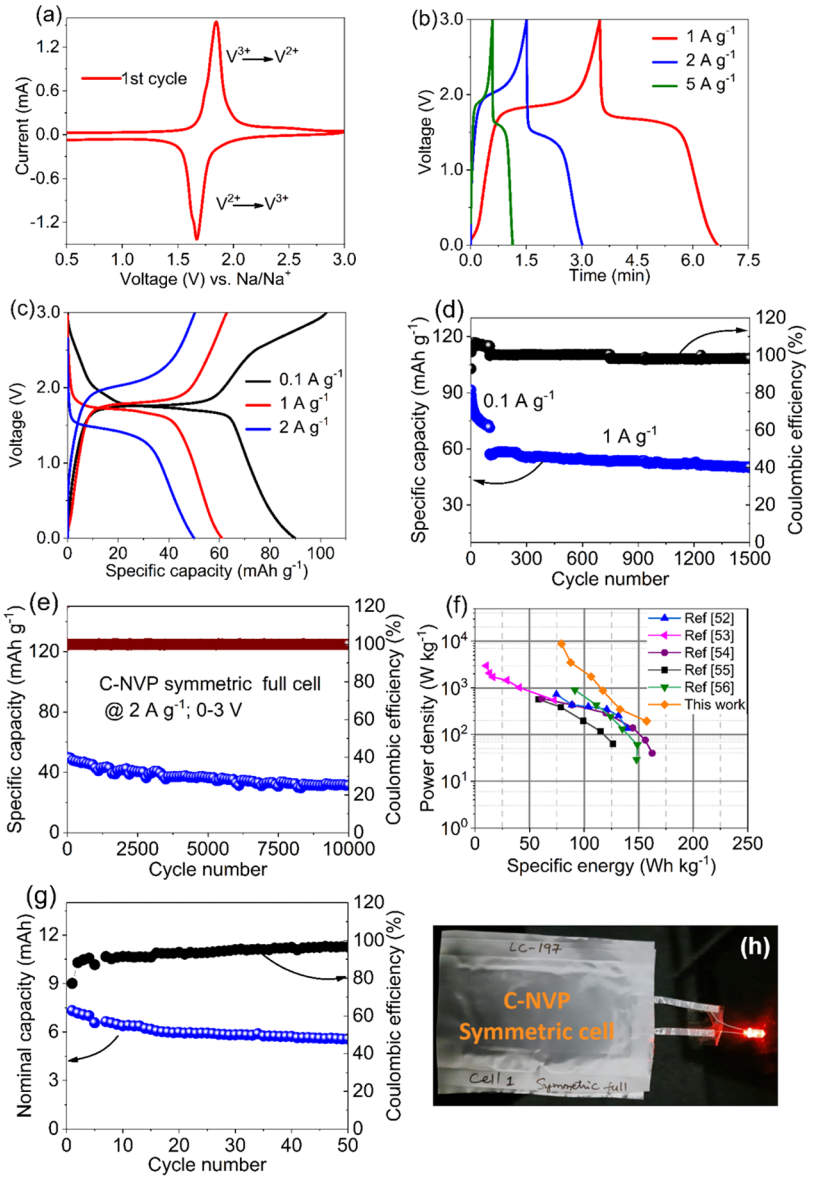

Figure 7. (a) Cyclic voltammogram of the C-NVP symmetric full cell at 100 μV s^{-1}. (b,c) Galvanostatic charge−discharge curves of the C-NVP symmetric full cell at 0.1, 1, 2, and 5 A g^{-1} during the first cycle. (d) Cyclic stability of the C-NVP symmetric full cell at 0.1 and 1 A g^{-1}. (e) Long-term cycling study at 2 A g^{-1}. (f) Ragone plot for the C-NVP symmetric full cell at different current densities. (g) Nominal capacity *vs* cycle number plot of the symmetric pouch cell. (h) Symmetric pouch cell of ∼1.8 V with glowing red LED.

exhibited by C-NVP at 1 A g^{-1} (8.5 C) without compromising on the power density (1743 W kg^{-1}) as shown in the Ragone plot (Figure 7f). A symmetric pouch cell fabricated using the C-NVP displayed a cell voltage of 1.8 V with a ∼7 mA h nominal capacity glowed a red LED light (Figure 7g,h). The studies in literature until now have followed a cathode to anode ratio of 1:2, which leads to excess mass loading on the anode side, resulting in the increase of cell weight as well as unnecessary side reactions due to the excess Na^+ ions coming out of the anode.[54−56] The optimized mass loading of 1:1 is sufficient enough to achieve good performance in the cell level. A shell kind of mesoporous carbon-encapsulated NVP synthesized through the microwaves exhibited specific energy and power density values (Table S3) superior to those of the pristine,[51,52] congeneric,[53] codoped,[54] rGO-based,[55] and expanded graphite-based[56] NVP symmetric cells reported earlier (Figure 7f).

4. CONCLUSIONS

In summary, a simple, fast, and scalable microwave-assisted sol−gel route has been employed to synthesize the *in situ* carbon-coated $Na_3V_2(PO_4)_3$ (C-NVP) cathode embedded in a 3D mesoporous carbon matrix. Such a robust microstructure has been optimized through the gelation time and content of citric acid. C-NVP has delivered specific capacities of 112 and 102 mA h g^{-1} at 0.1 and 1 C-rates, respectively, with enhanced cyclic stability when cycled between 2.3 and 3.9 V. In addition, the robust microstructure provides cyclic stability at a wider potential window with a very high specific capacity of ∼143 mA h g^{-1} with 75% retention after 500 cycles at 1.0 C-rate, resulting in enhancement of specific energy. *In situ* synthesized mesoporous carbon acted as a buffer and resisted the volume expansions during the complete $[Na_4V_2(PO_4)_3]$ and partial sodiation $[Na_{3.5}V_2(PO_4)_3]$ in the NVP structure. A symmetric SIB utilizing C-NVP as both cathode and anode resulted in

https://doi.org/10.1021/acsaem.1c02367
ACS Appl. Energy Mater. 2021, 4, 12581−12592

excellent rate performance and long cycle life. It has delivered a high specific capacity of 50 mA h g^{-1} at 2 A g^{-1} (17 C-rate), corresponding to a specific energy of 88 W h kg^{-1} and a power density of 3504 W kg^{-1} with cyclic stability > 10,000 cycles. An enhanced Na^+-ion diffusivity of 3.97−5.22 × 10^{-10} cm^2 s^{-1} has been observed due to the synergetic effect of 3D mesoporous carbon obtained during the synthesis, which can enable to prepare high-power sodium-ion batteries (SIBs) using the synthesized C-NVP electrode material. Our approach of scalable and fast synthesis of the $Na_3V_2(PO_4)_3$ electrode with a robust microstructure, which provides a high specific energy and power density with a long cycle life, can open up the possibility of its application in the future.

■ ASSOCIATED CONTENT

Supporting Information

The Supporting Information is available free of charge at https://pubs.acs.org/doi/10.1021/acsaem.1c02367.

Additional data of calculations, synthesis mechanism, FTIR, comparison data with the literature, EDS elemental mapping, Scherrer equation, confocal Raman imaging, additional cyclic voltammogram, and convex hull plot (PDF)

■ AUTHOR INFORMATION

Corresponding Author

Bijoy Das − *Centre for Automotive Energy Materials (CAEM), International Advanced Research Centre for Powder Metallurgy and New Materials (ARCI), Chennai 600113 Tamil Nadu, India;* orcid.org/0000-0002-3213-667X; Phone: +914466632807; Email: bijoydas@arci.res.in

Authors

P. Laxman Mani Kanta − *Centre for Automotive Energy Materials (CAEM), International Advanced Research Centre for Powder Metallurgy and New Materials (ARCI), Chennai 600113 Tamil Nadu, India; Department of Metallurgical and Materials Engineering, Indian Institute of Technology Madras (IITM), Chennai 600036 Tamil Nadu, India*

N. Lakshmi Priya − *Centre for Automotive Energy Materials (CAEM), International Advanced Research Centre for Powder Metallurgy and New Materials (ARCI), Chennai 600113 Tamil Nadu, India*

Prajeet Oza − *Atomistic Modelling and Materials Design Group, Indian Institute of Technology Madras (IITM), Chennai 600036 Tamil Nadu, India; Department of Metallurgical and Materials Engineering, Indian Institute of Technology Madras (IITM), Chennai 600036 Tamil Nadu, India*

M. Venkatesh − *Centre for Automotive Energy Materials (CAEM), International Advanced Research Centre for Powder Metallurgy and New Materials (ARCI), Chennai 600113 Tamil Nadu, India*

Satyesh Kumar Yadav − *Atomistic Modelling and Materials Design Group, Indian Institute of Technology Madras (IITM), Chennai 600036 Tamil Nadu, India; Department of Metallurgical and Materials Engineering, Indian Institute of Technology Madras (IITM), Chennai 600036 Tamil Nadu, India*

G. Sundararajan − *Centre for Automotive Energy Materials (CAEM), International Advanced Research Centre for Powder Metallurgy and New Materials (ARCI), Chennai 600113 Tamil Nadu, India*

R. Gopalan − *Centre for Automotive Energy Materials (CAEM), International Advanced Research Centre for Powder Metallurgy and New Materials (ARCI), Chennai 600113 Tamil Nadu, India;* orcid.org/0000-0003-2871-8682

Complete contact information is available at: https://pubs.acs.org/10.1021/acsaem.1c02367

Author Contributions

The manuscript was written through contributions of all authors. All authors have given approval to the final version of the manuscript.

Notes

The authors declare no competing financial interest.

■ ACKNOWLEDGMENTS

The authors would like to acknowledge the financial support from the Department of Science and Technology through Technical Research Centre (TRC project: AI/1/65/ARCI/2014) and DST project: DST/TMD/MES/2K17/46, Government of India, for the completion of the work. The authors would like to acknowledge Dr. Neha Hebalkar for carrying out the XPS analysis. The authors also like to thank Late Dr. G. Padmanabham, Director, ARCI, and Dr. Tata Narasinga Rao, Director (Additional charge), ARCI, for allowing us to carry out this work with continuous support.

■ REFERENCES

(1) Barpanda, P.; Lander, L.; Nishimura, S.-i.; Yamada, A. Polyanionic Insertion Materials for Sodium-Ion Batteries. *Adv. Energy Mater.* **2018**, *8*, 1703055.

(2) Ni, Q.; Bai, Y.; Wu, F.; Wu, C. Polyanion-type electrode materials for sodium-ion batteries. *Adv. Sci.* **2017**, *4*, 1600275.

(3) You, Y.; Manthiram, A. Progress in High-Voltage Cathode Materials for Rechargeable Sodium-Ion Batteries. *Adv. Energy Mater.* **2018**, *8*, 1701785.

(4) Ma, J.-M.; Li, Y.-T. Editorial for advanced energy storage and conversion materials and technologies. *Rare Met.* **2021**, *40*, 246−248.

(5) Rajagopalan, R.; Zhang, Z.; Tang, Y.; Jia, C.; Ji, X.; Wang, H. Understanding Crystal Structures, Ion Diffusion Mechanisms and Sodium Storage Behaviors of NASICON Materials. *Energy Storage Mater.* **2021**, *34*, 171−193.

(6) Wang, Q.; Zhang, M.; Zhou, C.; Chen, Y. Concerted Ion-Exchange Mechanism for Sodium Diffusion and Its Promotion in $Na_3V_2(PO_4)_3$ Framework. *J. Phys. Chem. C* **2018**, *122*, 16649−16654.

(7) Song, W.; Cao, X.; Wu, Z.; Chen, J.; Huangfu, K.; Wang, X.; Huang, Y.; Ji, X. A study into the extracted ion number for NASICON structured $Na_3V_2(PO_4)_3$ in sodium-ion batteries. *Phys. Chem. Chem. Phys.* **2014**, *16*, 17681−17687.

(8) Jian, Z.; Zhao, L.; Pan, H.; Hu, Y.-S.; Li, H.; Chen, W.; Chen, L. Carbon coated $Na_3V_2(PO_4)_3$ as novel electrode material for sodium ion batteries. *Electrochem. Commun.* **2012**, *14*, 86−89.

(9) Tao, S.; Cui, P.; Huang, W.; Yu, Z.; Wang, X.; Wei, S.; Liu, D.; Song, L.; Chu, W. Sol−gel design strategy for embedded $Na_3V_2(PO_4)_3$ particles into carbon matrices for high-performance sodium-ion batteries. *Carbon* **2016**, *96*, 1028−1033.

(10) Chen, H.; Zhang, B.; Wang, X.; Dong, P.; Tong, H.; Zheng, J.-c.; Yu, W.; Zhang, J. CNT-decorated $Na_3V_2(PO_4)_3$ microspheres as a high-rate and cycle-stable cathode material for sodium ion batteries. *ACS Appl. Mater. Interfaces* **2018**, *10*, 3590−3595.

(11) Zhou, Y.-X.; Zhang, L.-L.; Yang, X.-L.; Huang, Y.-H.; Ding, X.-K.; Ma, D.; Wang, J.-Q. Synthesis of Nano sheet-structured $Na_3V_2(PO_4)_3$/C as high-performance cathode material for sodium

ion batteries using anthracite as carbon source. *Ceram. Int.* **2017**, *43*, 2333−2337.
(12) Wang, E.; Xiang, W.; Rajagopalan, R.; Wu, Z.; Yang, J.; Chen, M.; Zhong, B.; Dou, S. X.; Chou, S.; Guo, X.; Kang, Y.-M. Construction of 3D pomegranate-like $Na_3V_2(PO_4)_3$/conducting carbon composites for high-power sodium-ion batteries. *J. Mater. Chem. A* **2017**, *5*, 9833−9841.
(13) Ren, W.; Yao, X.; Niu, C.; Zheng, Z.; Zhao, K.; An, Q.; Wei, Q.; Yan, M.; Zhang, L.; Mai, L. Cathodic polarization suppressed sodium-ion full cell with a 3.3 V high-voltage. *Nano Energy* **2016**, *28*, 216−223.
(14) Wang, D.; Chen, N.; Li, M.; Wang, C.; Ehrenberg, H.; Bie, X.; Wei, Y.; Chen, G.; Du, F. $Na_3V_2(PO_4)_3$/C composite as the intercalation-type anode material for sodium-ion batteries with superior rate capability and long-cycle life. *J. Mater. Chem. A* **2015**, *3*, 8636−8642.
(15) Mao, J.; Luo, C.; Gao, T.; Fan, X.; Wang, C. Scalable synthesis of $Na_3V_2(PO_4)_3$/C porous hollow spheres as a cathode for Na-ion batteries. *J. Mater. Chem. A* **2015**, *3*, 10378−10385.
(16) Si, L.; Yuan, Z.; Hu, L.; Zhu, Y.; Qian, Y. Uniform and continuous carbon coated sodium vanadium phosphate cathode materials for sodium-ion battery. *J. Power Sources* **2014**, *272*, 880−885.
(17) Li, S.; Ge, P.; Zhang, C.; Sun, W.; Hou, H.; Ji, X. The electrochemical exploration of double carbon-wrapped $Na_3V_2(PO_4)_3$: Towards long-time cycling and superior rate sodium-ion battery cathode. *J. Power Sources* **2017**, *366*, 249−258.
(18) Didwal, P. N.; Verma, R.; Min, C.-W.; Park, C.-J. Synthesis of 3-dimensional interconnected porous $Na_3V_2(PO_4)_3$@ C composite as a high-performance dual electrode for Na-ion batteries. *J. Power Sources* **2019**, *413*, 1−10.
(19) Balaji, S.; Mutharasu, D.; Sankara Subramanian, N.; Ramanathan, K. A review on microwave synthesis of electrode materials for lithium-ion batteries. *Ionics* **2009**, *15*, 765.
(20) Beninati, S.; Damen, L.; Mastragostino, M. MW-assisted synthesis of $LiFePO_4$ for high power applications. *J. Power Sources* **2008**, *180*, 875−879.
(21) Yang, G.; Liu, H.; Ji, H.; Chen, Z.; Jiang, X. Microwave solid-state synthesis and electrochemical properties of carbon-free $Li_3V_2(PO_4)_3$ as cathode materials for lithium batteries. *Electrochim. Acta* **2010**, *55*, 2951−2957.
(22) Gawande, M. B.; Shelke, S. N.; Zboril, R.; Varma, R. S. Microwave-assisted chemistry: synthetic applications for rapid assembly of nanomaterials and organics. *Acc. Chem. Res.* **2014**, *47*, 1338−1348.
(23) Zhu, Y.-J.; Chen, F. Microwave-assisted preparation of inorganic nanostructures in liquid phase. *Chem. Rev.* **2014**, *114*, 6462−6555.
(24) Dallinger, D.; Kappe, C. O. Microwave-assisted synthesis in water as solvent. *Chem. Rev.* **2007**, *107*, 2563−2591.
(25) Bao, S.-J.; Liang, Y.-Y.; Li, H.-L. Synthesis and electrochemical properties of $LiMn_2O_4$ by microwave-assisted sol−gel method. *Mater. Lett.* **2005**, *59*, 3761−3765.
(26) Bao, S.-J.; Liang, Y.-Y.; Zhou, W.-J.; He, B.-L.; Li, H.-L. Synthesis and electrochemical properties of $LiAl_{0.1}Mn_{1.9}O_4$ by microwave-assisted sol−gel method. *J. Power Sources* **2006**, *154*, 239−245.
(27) Suryakala, K.; Marikkannu, K. R.; Paruthimal Kalaignan, G.; Vasudevan, T. Synthesis and characterization of $LiCo_xMn_{2-x}O_4$ powder by a novel CAM microwave-assisted sol−gel method for Li ion battery. *J. Solid State Electrochem.* **2007**, *11*, 1671−1677.
(28) Yao, J.; Jia, Z.; Zhang, P.; Shen, C.; Wang, J.; Aguey-Zinsou, K.-F.; Ma, C.; Wang, L. Microwave assisted sol−gel synthesis of chlorine doped lithium vanadium phosphate. *Ceram. Int.* **2013**, *39*, 2165−2170.
(29) Wei, C.; Luo, F.; Zhang, C.; Gao, H.; Niu, J.; Ma, W.; Bai, Y.; Zhang, Z. Voltage window-dependent electrochemical performance and reaction mechanisms of $Na_3V_2(PO_4)_3$ cathode for high-capacity sodium ion batteries. *Ionics* **2020**, *26*, 2343−2351.
(30) Kang, J.; Baek, S.; Mathew, V.; Gim, J.; Song, J.; Park, H.; Chae, E.; Rai, A. K.; Kim, J. High rate performance of a $Na_3V_2(PO_4)_3$/C cathode prepared by pyro-synthesis for sodium-ion batteries. *J. Mater. Chem.* **2012**, *22*, 20857−20860.
(31) Xu, J.; Chen, J.; Zhou, S.; Han, C.; Xu, M.; Zhao, N.; Wong, C.-P. Sequentially-processed $Na_3V_2(PO_4)_3$ for cathode material of aprotic sodium ion battery. *Nano Energy* **2018**, *50*, 323−330.
(32) Lim, S. Y.; Kim, H.; Shakoor, R. A.; Jung, Y.; Choi, J. W. Electrochemical and thermal properties of NASICON structured $Na_3V_2(PO_4)_3$ as a sodium rechargeable battery cathode: a combined experimental and theoretical study. *J. Electrochem. Soc.* **2012**, *159*, A1393−A1397.
(33) Jian, Z.; Yuan, C.; Han, W.; Lu, X.; Gu, L.; Xi, X.; Hu, Y.-S.; Li, H.; Chen, W.; Chen, D.; Ikuhara, Y.; Chen, L. Atomic Structure and Kinetics of NASICON $Na_xV_2(PO_4)_3$ Cathode for Sodium-Ion Batteries. *Adv. Funct. Mater.* **2014**, *24*, 4265−4272.
(34) Song, W.; Ji, X.; Wu, Z.; Zhu, Y.; Yang, Y.; Chen, J.; Jing, M.; Li, F.; Banks, C. E. First exploration of Na-ion migration pathways in the NASICON structure $Na_3V_2(PO_4)_3$. *J. Mater. Chem. A* **2014**, *2*, 5358−5362.
(35) Holzwarth, U.; Gibson, N. The Scherrer equation versus the "Debye-Scherrer equation". *Nat. Nanotechnol.* **2011**, *6*, 534.
(36) Leofanti, G.; Padovan, M.; Tozzola, G.; Venturelli, B. Surface area and pore texture of catalysts. *Catal. Today* **1998**, *41*, 207−219.
(37) Liu, X.; Enhui, W.; Feng, G.; Wu, Z.; Xiang, W.; Guo, X.; Li, J.; Zhong, B.; Zheng, Z. Compared investigation of carbon-decorated $Na_3V_2(PO_4)_3$ with saccharides of different molecular weights as cathode of sodium ion batteries. *Electrochim. Acta* **2018**, *286*, 230−241.
(38) Wei, T.; Yang, G.; Wang, C. Bottom−up assembly of strongly−coupled $Na_3V_2(PO_4)_3$/C into hierarchically porous hollow nanospheres for high−rate and−stable Na-ion storage. *Nano Energy* **2017**, *39*, 363−370.
(39) Feng, P.; Wang, W.; Wang, K.; Cheng, S.; Jiang, K. $Na_3V_2(PO_4)_3$/C synthesized by a facile solid-phase method assisted with agarose as a high-performance cathode for sodium-ion batteries. *J. Mater. Chem. A* **2017**, *5*, 10261−10268.
(40) Masquelier, C.; Wurm, C.; Rodríguez-Carvajal, J.; Gaubicher, J.; Nazar, L. A powder neutron diffraction investigation of the two rhombohedral NASICON analogues: γ-$Na_3Fe_2(PO_4)_3$ and $Li_3Fe_2(PO_4)_3$. *Chem. Mater.* **2000**, *12*, 525−532.
(41) Zheng, L.-L.; Xue, Y.; Hao, S.-E.; Wang, Z.-b. Porous $Na_3V_2(PO_4)_3$ prepared by freeze-drying method as high performance cathode for sodium-ion batteries. *Ceram. Int.* **2018**, *44*, 9880−9886.
(42) Oh, J. A. S.; He, H.; Sun, J.; Cao, X.; Chua, B.; Huang, Y.; Zeng, K.; Lu, L. Dual-Nitrogen-Doped Carbon Decorated on $Na_3V_2(PO_4)_3$ to Stabilize the Intercalation of Three Sodium Ions. *ACS Appl. Energy Mater.* **2020**, *3*, 6870−6879.
(43) Wang, X.-K.; Shi, J.; Mi, L.-W.; Zhai, Y.-P.; Zhang, J.-Y.; Feng, X.-M.; Wu, Z.-J.; Chen, W.-H. Hierarchical porous hard carbon enables integral solid electrolyte interphase as robust anode for sodium-ion batteries. *Rare Met.* **2020**, *39*, 1053−1062.
(44) Wang, J.; Wang, Y.; Seo, D. H.; Shi, T.; Chen, S.; Tian, Y.; Kim, H.; Ceder, G. A High-Energy NASICON-Type Cathode Material for Na-Ion Batteries. *Adv. Energy Mater.* **2020**, *10*, 1903968.
(45) Rui, X. H.; Ding, N.; Liu, J.; Li, C.; Chen, C. H. Analysis of the chemical diffusion coefficient of lithium ions in $Li_3V_2(PO_4)_3$ cathode material. *Electrochim. Acta* **2010**, *55*, 2384−2390.
(46) Li, G.; Jiang, D.; Wang, H.; Lan, X.; Zhong, H.; Jiang, Y. Glucose-assisted synthesis of $Na_3V_2(PO_4)_3$/C composite as an electrode material for high-performance sodium-ion batteries. *J. Power Sources* **2014**, *265*, 325−334.
(47) Jian, Z.; Sun, Y.; Ji, X. A new low-voltage plateau of $Na_3V_2(PO_4)_3$ as an anode for Na-ion batteries. *Chem. Commun.* **2015**, *51*, 6381−6383.
(48) Li, S.; Dong, Y.; Xu, L.; Xu, X.; He, L.; Mai, L. Effect of carbon matrix dimensions on the electrochemical properties of $Na_3V_2(PO_4)_3$ nanograins for high-performance symmetric sodium-ion batteries. *Adv. Mater.* **2014**, *26*, 3545−3553.

https://doi.org/10.1021/acsaem.1c02367
ACS Appl. Energy Mater. 2021, 4, 12581−12592

(49) Wang, S.; Zhao, J.; Wang, L.; Liu, X.; Wu, Y.; Xu, J. High performance $Na_3V_2(PO_4)_3$/C composite electrode for sodium-ion capacitors. *Ionics* **2015**, *21*, 2633−2638.
(50) Bag, S.; Zhou, C.; Reid, S.; Butler, S.; Thangadurai, V. Electrochemical studies on symmetric solid-state Na-ion full cell using $Na_3V_2(PO_4)_3$ electrodes and polymer composite electrolyte. *J. Power Sources* **2020**, *454*, 227954.
(51) Plashnitsa, L. S.; Kobayashi, E.; Noguchi, Y.; Okada, S.; Yamaki, J.-i. Performance of NASICON symmetric cell with ionic liquid electrolyte. *J. Electrochem. Soc.* **2010**, *157*, A536−A543.
(52) Zhang, Y.; Zhao, H.; Du, Y. Symmetric full cells assembled by using self-supporting $Na_3V_2(PO_4)_3$ bipolar electrodes for superior sodium energy storage. *J. Mater. Chem. A* **2016**, *4*, 7155−7159.
(53) Yao, X.; Zhu, Z.; Li, Q.; Wang, X.; Xu, X.; Meng, J.; Ren, W.; Zhang, X.; Huang, Y.; Mai, L. 3.0 V High Energy Density Symmetric Sodium-Ion Battery: $Na_4V_2(PO_4)_3$‖$Na_3V_2(PO_4)_3$. *ACS Appl. Mater. Interfaces* **2018**, *10*, 10022−10028.
(54) Das, A.; Majumder, S. B.; Chaudhuri, A. R. K^+ and Mg^{2+} co-doped bipolar Na_3V_2 $(PO_4)_3$: An ultrafast electrode for symmetric sodium ion full cell. *J. Power Sources* **2020**, *461*, 228149.
(55) Wang, W.; Xu, Q.; Liu, H.; Wang, Y.; Xia, Y. A flexible symmetric sodium full cell constructed using the bipolar material $Na_3V_2(PO_4)_3$. *J. Mater. Chem. A* **2017**, *5*, 8440−8450.
(56) Gu, E.; Xu, J.; Du, Y.; Ge, X.; Zhu, X.; Bao, J.; Zhou, X. Understanding the influence of different carbon matrix on the electrochemical performance of $Na_3V_2(PO_4)_3$ cathode for sodium-ion batteries. *J. Alloys Compd.* **2019**, *788*, 240−247.

https://doi.org/10.1021/acsaem.1c02367
ACS Appl. Energy Mater. 2021, 4, 12581−12592